Energy Storage Materials 63 (2023) 102975

Contents lists available at ScienceDirect

Energy Storage Materials

journal homepage: www.elsevier.com/locate/ensm

Molecular carbon skeleton with self−regulating ion−transport channels for long−life potassium ion batteries

Wencong Feng [a,#], Chuanqi Pan [b,#], Hong Wang [a,c,#], Biluan Zhang [b], Wen Luo [d,*], Chunli Shen [a], Junjun Wang [a], Chaojie Cheng [a], Xianmin Xv [a], Ruohan Yu [a,c], Yanbing Guo [b,e,f,*], Liqiang Mai [a,g,*]

[a] State Key Laboratory of Advanced Technology for Materials Synthesis and Processing, School of Materials Science and Engineering, Wuhan University of Technology, Wuhan 430070, PR China
[b] Key Laboratory of Pesticide & Chemical Biology of Ministry of Education, Institute of Environmental and Applied Chemistry, College of Chemistry, Central China Normal University, Wuhan 430079, PR China
[c] Nanostructure Research Center (NRC), Wuhan University of Technology, Wuhan 430070, PR China
[d] Department of Physics, School of Science, Wuhan University of Technology, Wuhan 430070, PR China
[e] Engineering Research Center of Photoenergy Utilization for Pollution Control and Carbon Reduction, Ministry of Education, Wuhan 430079, PR China
[f] Wuhan Institute of Photochemistry and Technology, Wuhan, 430082, PR China
[g] Hainan Institute, Wuhan University of Technology, Sanya 572000, PR China

ARTICLE INFO

Keywords:
Self-regulating ion-transport channels
Graphdiyne
Potassium−ion batteries
in situ TEM and Raman
Molecular carbon skeleton

ABSTRACT

Developing anode materials with multiple-dimensional ion transport channels, especially to overcome huge volume expansion and sluggish ion diffusion kinetics caused by large radius of potassium ion (K^+), is critical to improve the potassium storage performance. Herein, we propose a self-reversible conversion of chemical bonds with different bond lengths based on graphdiyne (GDY) to self-regulating the ion transport channels. Density functional theory (DFT) calculations and *ex/in situ* electrochemical tests proof the in−plane triangular−like pores (5.46 Å) of the GDY framework offer a transport channel for K^+ (1.38 Å) diffusion in the direction perpendicular to the GDY plane, which differs it from carbonaceous materials whose ion diffusion is mostly governed by in−plane migration. Furthermore, the reversible alkyne−alkene bonds linking/breaking of GDY stimulated by K^+ to realize self-regulating ion channels are demonstrated by in situ Raman and electro−kinetic analysis. Moreover, compared to graphite, the GDY anode with 2 orders of magnitude diffusion coefficient delivered a high reversible capacity of 202 mAh g^{-1} at 100 mA g^{-1} exhibited extraordinary durability corresponding to cycle time over 380 days. This work opens a new avenue of designing intelligent, efficient ion transport channels from molecular carbon skeleton perspective to enhance diffusion kinetic for high-performance KIBs.

1. Introduction

Potassium−ion batteries (KIBs) have emerged as next generation energy storage alternatives to lithium−ion batteries (LIBs) owing to the abundant potassium storage and small solvated potassium ions (K^+) [1–3]. Particularly, the redox potential of K^+/K (−2.93 V vs standard hydrogen electrode, SHE) is quite close to that of Li^+/Li (−3.04 V vs SHE), which allows wider operating voltage of KIBs [4–9]. Unfortunately, the larger atomic radius of K^+ (1.38 Å vs 0.76 Å for Li^+) would cause substantial volumetric deformation and sluggish diffusion kinetics for most current KIBs anode materials [10–12]. Therefore, the development of electrode materials, especially the anode side, to achieve rapid charge transfer dynamic, high structural robustness and excellent electrochemical performance is urgent but remains challenging.

Carbonaceous anodes, featured by adjustable structure, high conductivity and low redox potential, has been considered as promising materials for high−performance KIBs [10,13]. For example, Ji et al. demonstrated the reversible electrochemical insertion of K^+ into graphite to from a steady potassium intercalated graphite (KC_8), which further accelerates the research on KIBs [14]. However, the large size of

* Corresponding authors.
E-mail addresses: luowen_1991@whut.edu.cn (W. Luo), guoyanbing@mail.ccnu.edu.cn (Y. Guo), mlq518@whut.edu.cn (L. Mai).
# These authors contributed equally.

https://doi.org/10.1016/j.ensm.2023.102975
Received 2 July 2023; Received in revised form 20 August 2023; Accepted 13 September 2023
Available online 21 September 2023

K^+ arouses huge volumetric expansion (61% by KC_8 vs 10% by LiC_6), causing unstable crystal structure and sever capacity fading [15–17]. Moreover, due to the fixed pore size limitation of aromatic carbon ring in the graphite plane structure, the diffusion of K^+ perpendicular to two−dimensional (2D) plane is restricted (Scheme 1a) [18–20]. The K^+ can only be driven in the narrow interlayer planar lattice structure of graphite, thus leading to slow intrinsic diffusion kinetics and poor rate performance [21,22].

Compared to graphitic carbon, the emerging nanocarbon materials, including soft carbon [11], hard carbon [23–25], graphene [26,27] and so on, have been recognized as promising anodes for KIBs. Among them, researchers mainly focus on the mesoscopic structure regulation research of carbon structure (such as defect engineering, pore structures regulation, macro and micro morphology designing), to boost reversibly potassium storage via adsorption−induced capacitive behavior [28–32]. However, the behaviors at atomic-to-molecular level (such as electronic properties, junction effects, electrical interactions,) that are caused by K^+ stimulation on potassium storage remains at primary level [33,34]. Moreover, the capacitive behavior mainly occurs on surface or near surface region, e.g., accommodating K^+ by surface pores, voids, defects and functional groups [35,36]. Although the apparent diffusion kinetics of K^+ in reported capacitor−style carbon materials has been improved, the intrinsic K^+ transport inside the bulk electrode materials is still slow [37,38]. One of results caused by slow diffusion is that more K^+ accumulates on the surface, leading to larger volume change and stress concentration [39]. Consequently, rationally designing advanced carbon materials from the perspective of molecular carbon skeleton design with regard to promoting intrinsic ion diffusion dynamics and reducing volume change is of great significance.

Graphdiyne (GDY), a novel 2D carbon allotrope composed by sp and sp^2 hybrid carbon atoms, has drawn extensive attention to energy storage and conversion because of its facilitated appropriate layer spacing, ion transport pathway and excellent conductivity [40,41]. GDY is consists of hexagon benzene rings connected by diacetylenic linkages, with a large conjugated π−extended carbon framework and intrinsic 18−C in−plane triangular pores [42–44]. Recently, researchers have proved that in−plane pore can act as an out−of−plane transport channel for ions [45,46]. Liu et al. reported GDY skeleton by temperature−mediated engineering strategy and used it as the potassium storage anode for KIBs, and revealed the favorable adsorption sites of K^+ through first principles method [47]. Despite a few works have shown the superiority of GDY as anode materials for KIBs, the understanding of its potassium storage mechanism still depends on theoretical calculation. Especially, π−conjugated carbon framework, in−plane pores, chemical bonds conversion, crystal lattice distortion of GDY upon the action of K^+ are still unclear [48–50]. Therefore, it is highly desirable to ascertain ion transport mechanism of GDY to achieve rapid intrinsic diffusion of K^+, although still a great challenge.

Herein, we reported that a self−regulating ion channel based on the planar triangular hole of GDY provides additional transport pathways during potassiation\depotassiaion process, which improves the intrinsic diffusion kinetics of K^+ (Scheme 1b). *In situ* Raman, *ex situ X*−ray photoelectron spectroscopy (XPS) and DFT calculations reveal that the reversible conversion of alkyne−alkene bond with stimulus of K^+ caused the self−regulating of the ion transport channel in GDY. Galvanostatic intermittent titration technique (GITT) test suggest that self−regulating ion channel decreases the transport barrier of K^+ and improves the K^+ diffusion coefficient. Utilizing in situ transmission electron microscopy (TEM), the structural evolution of GDY during potassiation was systematically investigated. The GDY enables superior potassium storage performances with high capacity, outstanding cyclic stability (stable cycling more than 380 days with a high reversible capacity of 202 mAh g^{-1}, a decay of 0.012% per cycle with a high coulombic efficiency (CE) of 99.5%) and fast ion/electron−transport kinetics. The results show that GDY can overcome the limitations of slow diffusion and volume expansion caused by larger K^+. More importantly, this work provides a strategy to design fast ion transport channels with self-regulating feature and develop high-performance materials for energy storage.

2. Results and discussion

2.1. Physical properties of GDY

The microstructure of stripped GDY was detected (Fig. 1a). The TEM results showed that GDY presented a large area of 2D nanosheet structure, and it was difficult to avoid the existence of trace GDY powder with low exfoliation degree. With the statistical analysis of several different regions, the synthesized 2D nanosheet exfoliated GDY with a thickness of about ~ 0.8 nm (Fig. 1b-c), was evidenced by atomic force microscope (AFM). Based on literature reports and theoretical simulation results [51–53], it is shown that the thickness of GDY is ~ 0.8 nm, which corresponds to the three−layer stacked GDY layered structure [41,54]. The layered structure of GDY was also confirmed by the high−resolution TEM (HR−TEM). The interlayer distance of GDY is about 0.378 nm, corresponding to the characteristic value for the multilayer GDY (Fig. 1d). Fig. 1e presents the HAADF−STEM image of GDY. The results

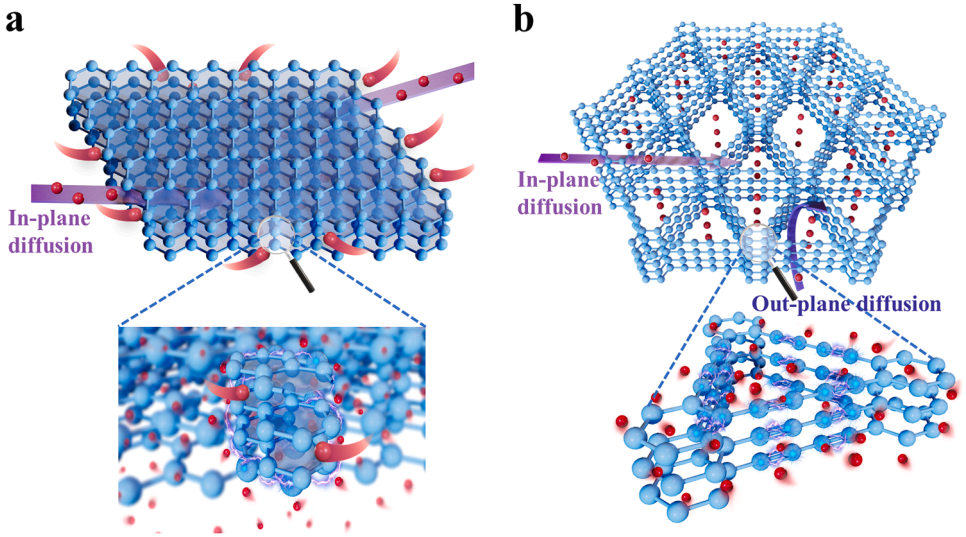

Scheme 1. Illustration for the structural features of graphite (a) and GDY (b) on potassium ions transport and storages.

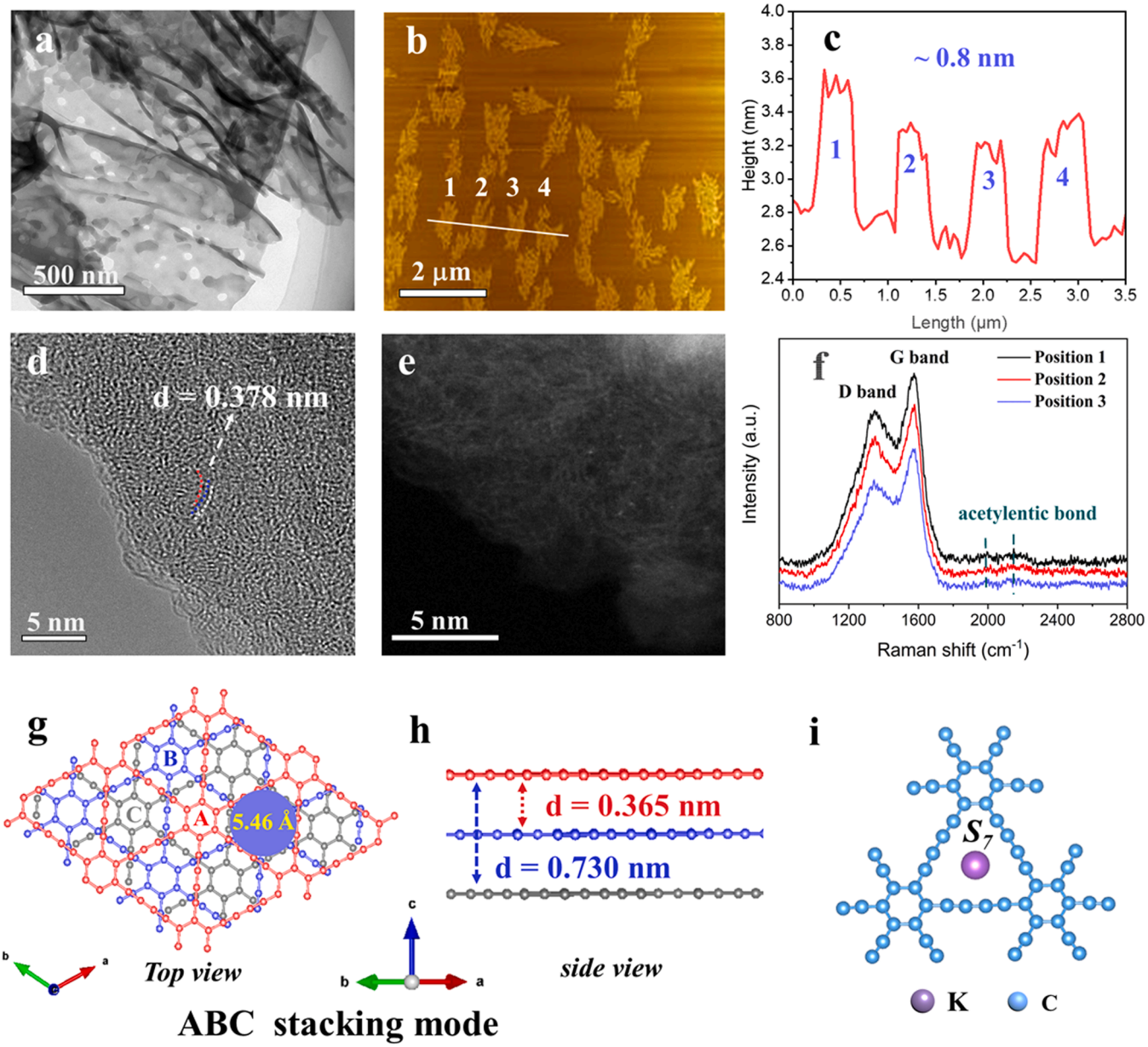

Fig. 1. (a) The TEM image of GDY. (b) The AFM image of GDY. (c) The thickness of GDY. (d) HR−TEM image of GDY. (e) HAADF−STEM image of GDY. (f) The Raman spectra of GDY. (g) The three layers GDY with "ABC" stacking mode. (h) The thickness of three layers GDY with "ABC" stacking mode. (i) Chemical structure of GDY and the most preferred K adsorption sites at triangular−like pores (Site 7). Other possible adsorption sites of K atom are summarized in Table S1.

show that GDY shows a clear layered structure, which is well consistent with the HR−TEM results. Fig. 1f shows typical Raman spectra of GDY at different positions. All the Raman spectra from different positions exhibited four prominent peaks at 1360 cm^{-1}, 1582 cm^{-1}, 1986 cm^{-1} and 2122 cm^{-1}, respectively [55]. The peak at 1986 cm^{-1} and 2122 cm^{-1} are attributed the conjugated acetylenic bonds [56]. The rich acetylenic bonds, unique pores (diameter of inscribed circle of triangular hole, 5.46 Å) and layered structure of GDY are not only conducive to the in−plane migration of potassium ions in the triangular pores [47], but also allow the diffusion of potassium ions between layers (Fig. 1g). X-ray photoelectron spectroscopy (XPS) indicate unambiguously that GDY is built exclusively from elemental carbon (Fig. S1). The high-resolution C 1 s signals of GDY can be readily deconvoluted into four contributing peaks at 284.6, 285.7, 287.6, 289.4 eV, which are assigned to C═C (sp^2), C≡C (sp), C—O, and C═O bonding, respectively. The X-ray diffraction (XRD) pattern (Fig. S2) showed broad peak centered at 22.5°, which agreed well with the typical representative peak of GDY [40].

GDY layer stack was analyzed to understand the role of bulk GDY structure in the potassium storage mechanism. The carbon atomic layer in bi−layer and tri−layer structures of GDY are stably stacked in "AB" and "ABC" mode of Bernal manner, respectively [41]. The DFT calculation results show that GDY tends to exist in the "ABC" three−layer stacking configuration, and the energy of its aggregate structure system is lower than that of the "AB" configuration [57]. The AFM and HR−TEM results show that the thickness of *e*−GDY is about 0.8 nm and it presents multilayer aggregation structure. For GDY with "ABC" stacking configuration (Fig. 1h-i), the distance between two carbon layers is 0.365 nm [58,59], and that between three layers is about 0.730 nm, which is consistent well with the results of AFM and HR−TEM. DFT calculations were carried out to evaluate the diffusion barrier of K^+ in different directions of GDY configuration (Fig. S3). As for the pristine GDY, the diffusion barrier for the in−plane diffusions between neighboring triangular−like pores is 0.8 eV. For out−of−plane diffusion of K^+ perpendicular to the 2D base plane, that is, triangular pores act as ion

transport channels (Fig. S4). The diffusion barrier in pristine GDY is 0.79 eV, while reduced to 0.58 eV in expanded pores with stimulus of K^+, highlighting that pores, especially expanded pores, will greatly facilitate the out−of−plane transport of K^+.

2.2. Structural and chemical bonds dynamic changes of GDY

In situ Raman test was then used to investigate the structural and chemical bonds dynamic changes of GDY. The peak at 1582 cm^{-1} (G band) corresponds to the first-order scattering of the E2g mode observed for in-phase stretching vibration sp^2 carbon. The peak at 1360 cm^{-1} (D band) is attributed to the breathing vibration of sp^2 carbon domain. As displayed in Fig. 2a-b, in initial discharge state I (open circuit voltage (OCV)−0.8 V): the intensity of G peak (1582 cm^{-1}) does not change, while the intensity of peak at conjugated acetylenic bonds (1986 cm^{-1} and 2122 cm^{-1}) has weakened, which can be regarded as the adsorption behavior of K^+ at diacetylenic triangular−like pores. Interestingly, G peak shifts to lower wavenumbers. The reason for this shift is that the π−electrons of alkyne partially transferred to the adsorbed K^+ and resulted in the transition of alkyne to bonds with alkene characteristics [60]. With appearance of more alkene feature, the in−plane C/C bonding stretching (C≡C—1.23 Å vs C═C—1.29 Å) increases the pore size of triangular pores and interlayer spacing, resulting in biaxial strain and leading to the redshift of G band [7]. With the continued discharge state II (0.8 V − 0.01 V): G peak shifted to higher wavenumbers (blue shift) with the intensity gradually decreased, which can be regarded as the interaction between the C—C/C═C bond with the inserted K^+. The appearance of blue shift is caused by the more inserted K^+ adsorbed into the triangular nanopores, resulting in the enlarging of pore size and the decrease of the interlayer spacing. With the potassium embedded, the steric hindrance and electron density are increased which reduces the corresponding electron-withdrawing ability and the electron deviation of benzene ring, leading to the blue shift of G band. At the same time, the further transition of alkyne to alkene after K^+ intercalation indicate the formation of a new transition state with extended conjugation [61]. The inherent large in−plane triangular pore of GDY can realize the diffusion of K^+ perpendicular to the basal plane. More importantly, the conversion of chemical bonds increases the pore size of K^+ transport channels, driving K^+ to realize rapid out−of−plane migration by expanding channels. During the subsequent charging state, the G peak first shifted to higher wavenumber and then to lower wavenumber, while the intensity of the G peak and acetylenic bonds increased gradually, indicating the reversible transition of the alkyne−alkene complex. This phenomenon is directly observed in the intensity map of the Raman spectra (Fig. 2d).

At the initial discharge process, the appearance of alkene feature provides more π-electrons with sp^2 characteristics, which means that the conjugation degree of sp^2 is changed, leading to the red shift of D band. With further potassiation process, the density of the benzene ring electron cloud increases, and more electrons need to be excited with greater energy, resulting in the blue shift of D band. Furthermore, the I_D/I_G ratios continuously increases from 0.90 to 0.99 upon potassation (Fig. S5), suggesting the increased defect density was caused by the transition of the alkyne−alkene. During charging process, the value of I_D/I_G recover to almost the initial level, confirming good self−reversible conversion of alkyne−alkene bonds with the K^+ response. In the subsequent charging and discharging process (Fig. S6), GDY still showed the dynamic behavior of realizing adjustable structure based on reversible chemical bond conversion.

Ex−situ XPS analysis was applied to understand the changes of conjugated acetylenic bonds constructed by sp−C atoms in the process of providing the storage sites for K^+. Fig. 2e illustrated the selected points under different potential at the initial discharge/charge process. From the high resolution XPS of C1s, two peaks at 285.3 and 284.8 eV correspond to the peaks of sp−C (C≡C) and sp^2−C (C—C). The intensity of sp−C peak gradually decreases, while the counterpart of sp^2−C peak increases with the decreased of potential, suggesting that acetylenic bond transforms to the intermediate bond with more alkene characteristics [62]. During gradually discharged process (Fig. S7a), the binding energies (BEs) of sp−C peak show obvious shift towards higher BEs compared with original state, further indicating that acetylenic bond participates in the process of K storage. In contrast, when recharging to 3 V (Fig. 2f and Fig. S7b), the GDY show shift towards lower BEs for the sp−C peak along with the intensity of sp^2−C decreasing and sp−C increasing, further verifying the reversible transition of the alkyne−alkene bonds, which is consistent with above in−situ Raman results. Besides the ratio of sp−C/ sp^2−C calculated from XPS integral area continuously decreases from 1.84 to 0.23 with the gradual potassiation process, then recovers to 1.57 when volage is above 3.0 V (Fig. 2g).

2.3. Electrochemical tests and analysis

The K^+ storage behaviors of GDY as an anode of potassium half cells was verified. Fig. 3a illustrated the initial cyclic voltammogram (CV) curves of GDY at a scan rate of 0.1 mV s^{-1}. During first scanning state, two wide irreversible cathodic peaks at 0.7 V and 0.45 V, correspond to reduction of electrolyte and formation of solid electrolyte interphase (SEI) film. Different from graphite electrodes (Fig. S8), a wide cathodic peak located at 1.1 V in the second cycle and then remained unchanged, indicating the in−plane nanopores of GDY absorb and accommodate K^+ [45]. The cathodic peaks at 0.25 V and 0.01 V represent the K storage by acetylenic bond and intercalation of K^+ to form K—C compounds. In the subsequent anodic process, the peaks at 0.35 V and 0.6 V are related to the extraction of K^+. The first galvanostatic charge−discharge (GCD) curves (Fig. S9) at 50 mA g^{-1} demonstrate similar behavior as the CV curves, where the initial CE is 26.2%. The cycling performances of GDY and corresponding CE are shown in Fig. 3b. GDY possesses high capacity of 220 mAh g^{-1} at 50 mA g^{-1} with the capacity retention of 85% from 20th to 600th cycles. The capacity retention rate is much higher than that of graphite, because GDY prosses self−regulating planar nanopores which combination of sp2 and sp−hybridized carbon, providing more K^+ storge sites and mitigating volume changes. Impressively, GDY demonstrated long−term cycling capability, stable cycling for more than 7 months at 50 mA g^{-1}, significantly higher than previously reported carbonaceous anodes (Table S2). The discharge/charge behaviors of GDY were further explored by GCD curves (Fig. 3c). The curves in the 100th and 600th cycles show sloping feature and overlap quite well, indicating good reversibility of ion storage behavior.

Fig. 3d displays the rate capabilities of GDY and graphite electrodes at different current densities. The capacities of GDY at 0.1, 0.2, 0.5, 1 and 2 A g^{-1} are 238, 208, 180, 157 and 131 mAh g^{-1}, respectively. Even at 5 A g^{-1}, GDY electrode could maintain high capacity of 101 mAh g^{-1}, corresponding to a high retention of 42% of the capacity at 0.1 A g^{-1}, while the corresponding capacity of graphite was only 8 mAh g^{-1}. Meanwhile, the capacity of 223 mAh g^{-1} can be recovered when the current density switches to 0.1 A g^{-1} again under a series of high−current rates, demonstrating superb stability of GDY. In addition, the GCD curves at various currents densities (Fig. 3e and Fig. S11) of GDY exhibit more stable voltage plateaus and smaller polarization than graphite, further confirming the outstanding rate capability. The observed small “plateau” in the beginning of charge process at high current density is actually due to a testing procedure issue in the constant current charge-discharge test. Impressively, GDY electrode can deliver a charge capacity of 109 mAh g^{-1} at 500 mA g^{-1} over 600 cycles, even remain high capacity of 83 mAh g^{-1} at 1 A g^{-1} over 1600 consecutive cycles and nearly 100% CE (Fig. S12 and S13). Moreover, in the long−term cycle at 100 mA g^{-1}, the GDY electrode shows a cycle of up to 380 days and runs over 2100 cycles with a high reversible capacity of 202 mAh g^{-1}, a decay of 0.012% per cycle with a high CE of 99.5% (Fig. 3f). As shown in Fig. S14, the corresponding GCD curves in different cycles have no obvious change during the one year running time, delivering superior cycling stability for K^+ storage.

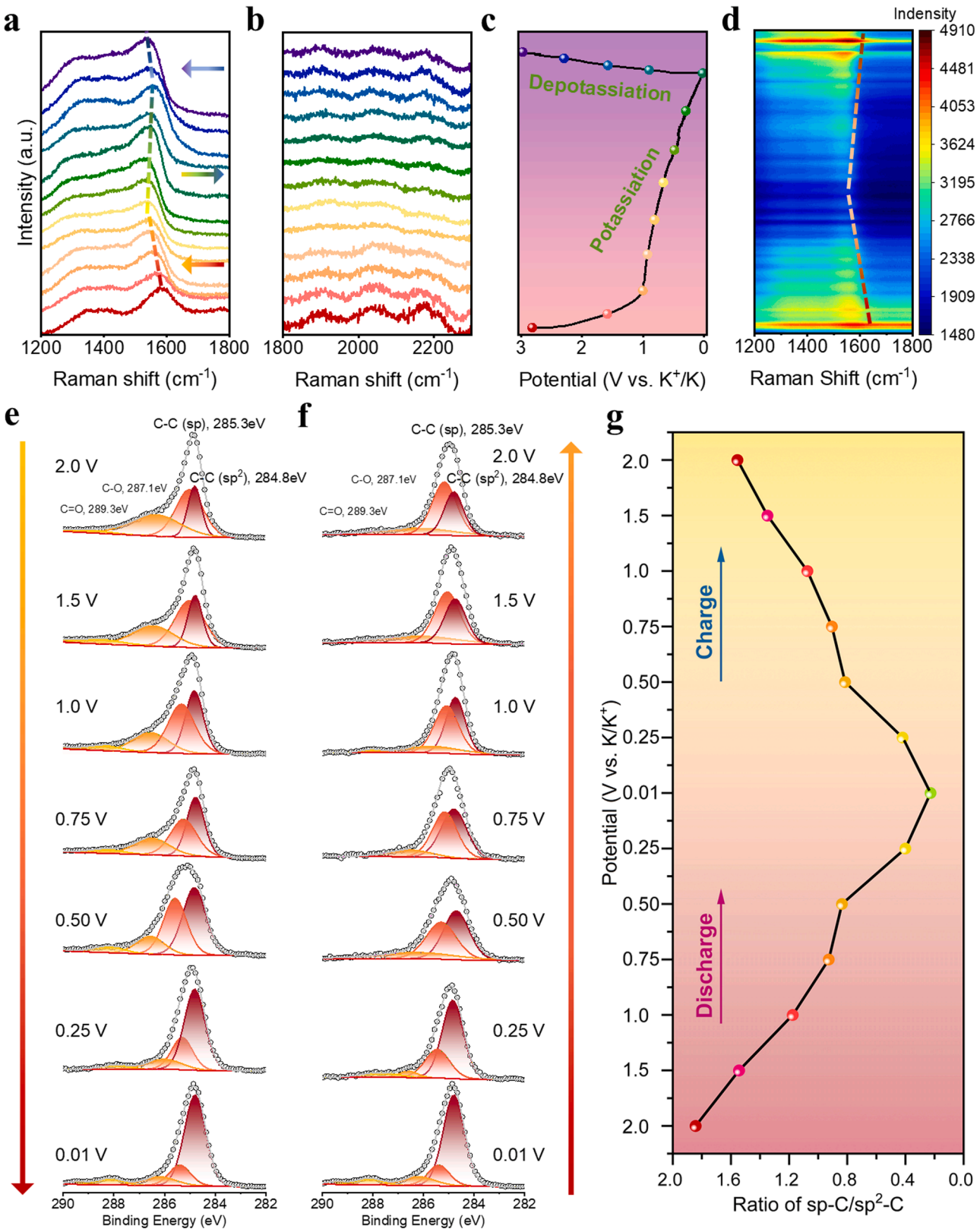

Fig. 2. (*a* – *d*) In situ Raman patterns and corresponding con-tour plots at various discharge–charge states. (a) Changes of G band during cycling; (b) changes of alkyne bonds during cycling; (c) first charge and discharge curves of GDY; (d) corresponding Raman mapping analysis of G bands changes during cycling. (*e* – *g*) Ex situ XPS measurements of the cycled electrodes at various discharge–charge states and corresponding evolution of sp−C/sp2−C ratio.

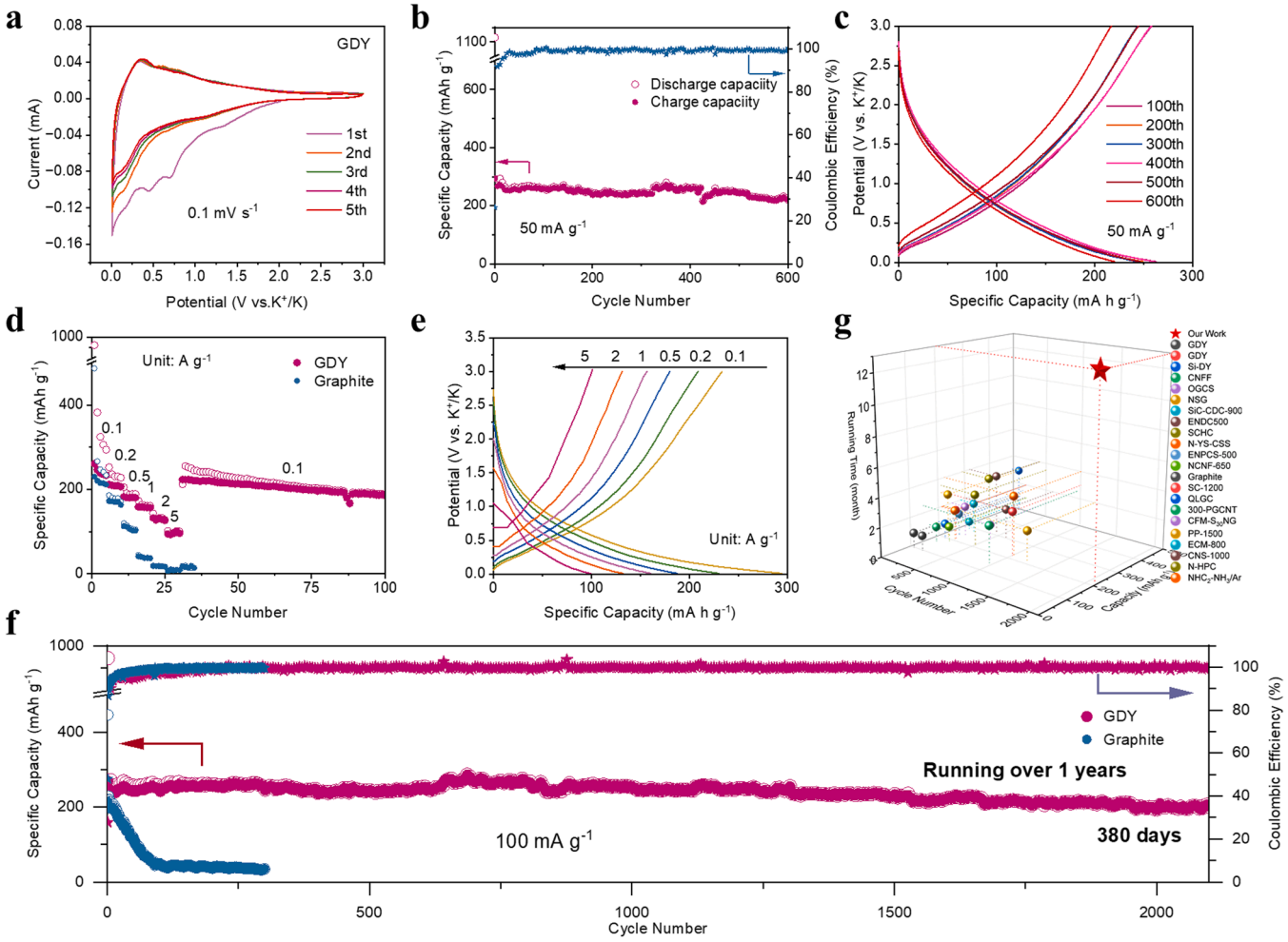

Fig. 3. Electrochemical performance of GDY and graphite in 0.01−3.0 V (vs. K^+/K). (a) CV curves of GDY at a scan rate of 0.1 mV s^{-1}. (b) Cycling performance at a current density of 0.1 A g^{-1}, (c) charge and discharge curves at 0.1 A g^{-1}. (d) Rate capabilities at current densities ranging from 0.1 to 5 A g^{-1} of the GDY and graphite electrode. (e) Charge and discharge curves at various current densities for GDY. (f) Long cyclic of the GDY and graphite electrodes at 0.1 A g^{-1}. (g) Comparison of rate and cycle performance of GDY anode with the reported other anode materials for KIBs.

Notably, compared to the recent literature works (Fig. 3g and Table S2), the excellent long−life capability of GDY for KIBs indeed surpassed the most of unmodified carbon−based composite anodes. From the above results, the long-term cycling performance and extraordinary capacity retention ability of the GDY electrode are obtained due to large interlayer distance (0.365 vs 0.335 nm of graphite), can mitigate the interlayer spacing change during cycling and facilitate the fast kinetics of K^+ intercalation [16]. Moreover, the abundant alkyne groups and in−plane nanopores combine with sp^2 and sp hybridized carbon afford strong interaction between K^+ and GDY and sufficient K^+ adsorption sites [43]. GDY can fix K^+ in its in−plane nanopores to alleviate the volume change caused by the intercalation behavior [63]. In addition, the self−regulating 18−C hexagon pores and layered structures of GDY are beneficial for the in−plane and out−of−plane ions diffusion, allowing K^+ to diffuse along the vertical 3D channels, which shortens the K^+ diffusion length and facilitates rapid ion diffusion within the electrode material [64]. On the contrary, due to the limitation of small pore size in molecular structure of graphite, the diffusion of K^+ perpendicular to the basal plane is blocked, leading to worse cycling performance [22].

2.4. K^+ reaction kinetics and diffusion behavior

To describe the reaction kinetics of the GDY, the CV tests were carried out at scan rates ranging from 0.1 to 2.0 mV/s. The CV curves in Fig. 4a manifest similar shapes and become broader with the increase of scan rates. The K^+ diffusion coefficient is investigated by the Randles−Sevcik equation [65]: $I_P = 2.69 \times 10^5 n^{3/2} A D_k^{1/2} v^{1/2} C_k$, which can be evaluated by linearly fitting the line of I_p versus $v^{1/2}$. In Fig. 4b, the slope of anodic and cathodic peaks of GDY were 0.0163 and 0.0138, respectively, much higher than those of graphite electrode (0.0079 and 0.0012). As shown in Fig. 4c, the K^+ diffusion coefficient at the anodic and cathodic of GDY calculated by equation were roughly one or two orders of magnitude greater than that of graphite respectively, indicating that GDY electrode delivered much faster ion transport dynamics over graphite. However, when calculating the chemical diffusion coefficient using CV method, only the peak current value is considered. This can only provide the apparent average chemical diffusion coefficient at the reaction potential corresponding to the peak current [66,67]. The electrode process kinetics differ slightly between potassium extraction and insertion. The diffusion coefficient obtained reflects the average chemical diffusion coefficient of potassium insertion/extraction near the peak current, but this method cannot determine the chemical diffusion coefficient at different potassium insertion levels. Due to the limitation of only measuring the apparent chemical diffusion coefficient, CV method cannot capture the variation of the diffusion coefficient with potassium content, which restricts its applicability.

Furthermore, GITT measurement was used to calculate the diffusion coefficient (D_k) under deep charge/discharge condition. For continuous

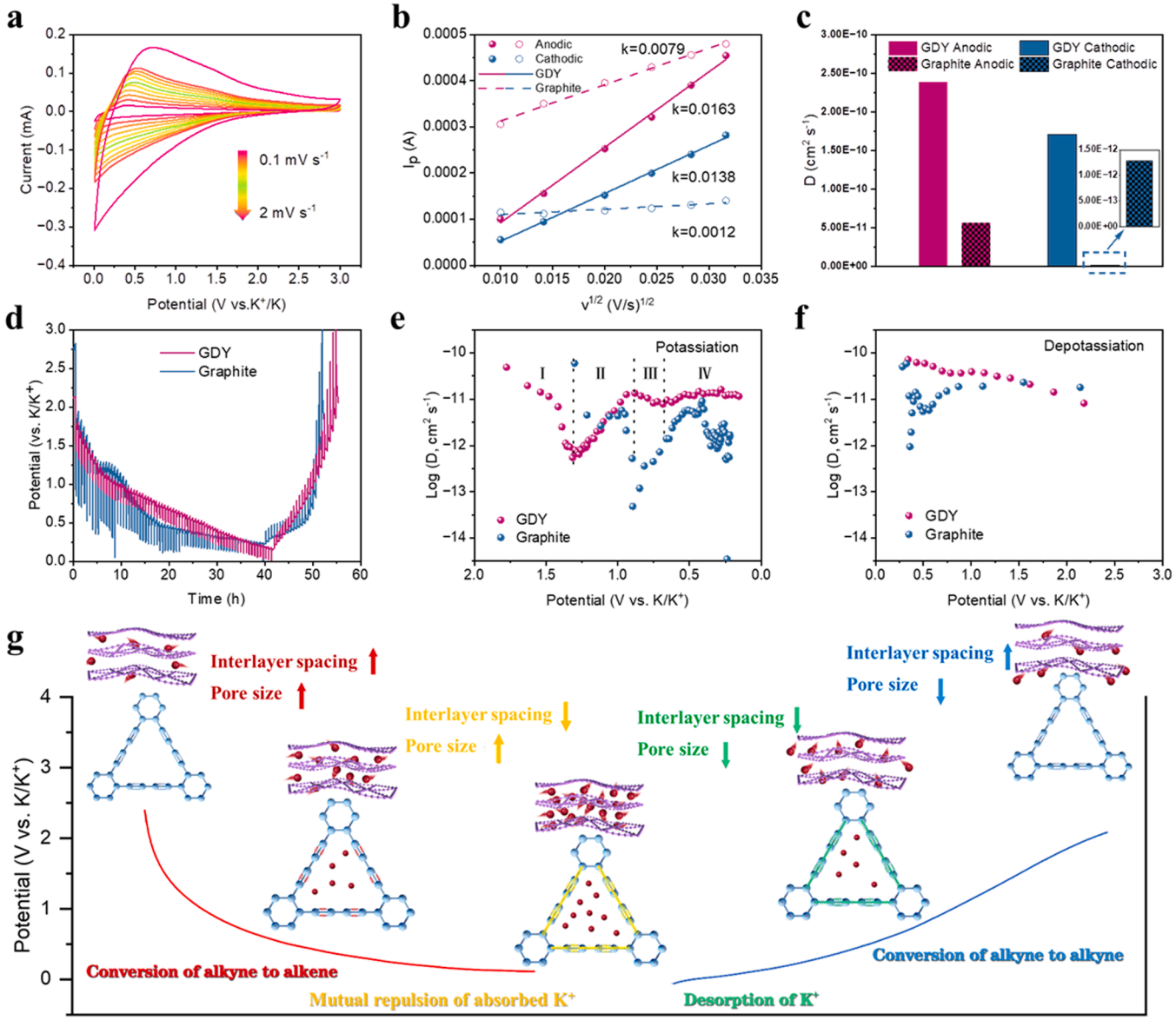

Fig. 4. Evaluations on K−ion diffusion kinetics. (a) CV curves of the GDY electrodes at sweep rates from 0.1 to 2.0 mV s^{-1}. (b) Reduction and Oxidation peak current versus $(V/s)^{1/2}$ and the corresponding linear fits. (c) The corresponding K^+ diffusion coefficient of GDY calculated by equation. (d) Galvanostatic intermittent titration technique (GITT) curves of GDY and graphite at the first cycle. (*e* − *f*) Diffusion coefficients of GDY and graphite calculated from the GITT profiles during the first potassiation/depotassiation cycle. (g) Schematic illustration of the reaction mechanism of GDY as an anode in KIBs.

electrochemical reactions involving the insertion and extraction of potassium ions, the chemical diffusion coefficient should vary with the extent of insertion/extraction. GITT can be used to measure the differences in diffusion coefficients of electrode materials for insertion and extraction in a relatively short period of time [68]. It allows for the determination of diffusion coefficient variations at different levels of potassium insertion/extraction, enabling in-depth investigation of the relationship between structure and kinetics [69]. Fig. 4d shows GDY exhibited smaller overpotentials compared to graphite, meaning a higher D_k. As shown in Fig. 4e, the D_k of GDY electrode significantly decreased at the range around I: 2.0 − 1.3 V. The rapid drop of D_k values could be attributed to the formation of SEI which consumes a large amount of K^+ [63]. The reverse increase of D_k values around the 1.3 − 0.9 V (II) due to the dynamic behavior of chemical bond conversion between alkyne and alkene under K^+ stimulation, which implies the triangular pore size of GDY increases and thus reduces the transport potential barrier of K^+. The D_k values decrease slightly at 0.9 − 0.7 V (III) corresponds to the K^+ intercalation into the GDY interlayer and transport between neighboring triangular pores. According to the results of DFT calculation, the high energy barrier of the in−plane diffusion reduces K^+ diffusion coefficient. With the insertion of additional K^+ (0.7 − 0.01 V, IV), more K^+ is adsorbed into the 18−C hexagon pores. The mutual repulsion of adsorbed K^+ on the triangular hole of butylene further increases the pore size, which promotes the out−of−plane migration of K^+ in the extended channels.

At the initial charging state (Fig. 4f), with the deintercalation of K^+, the expanded pores by repulsion gradually shrink, which prevents the diffusion of internal K^+ from GDY and leads to the gradual reduction of D_k. With the deep deintercalation of K^+, alkene spontaneously converts to alkyne, and the expanded pores gradually shrink to original state, resulting in a blockage of K^+ diffusion. The lower D_k values of graphite could be attributed to the K^+ diffusion through a non−regulatable two−dimensional (2D) layered structure, which seriously limits its diffusion rate. *In situ* XRD proves the reversible interlayer changes (Fig. S17). The diffraction peak (~ 25°) shifts negatively to a small angle from the original state until the discharge to 0.5 V then positively to a

high angle during subsequent continuous discharge to 0.01 V. At the charge process, the diffraction peak (~25°) undergoes a reversible shifting process.

Electrochemical impedance spectroscopy (EIS) was employed to study the charge−transfer resistance and explain the detailed electrochemical reaction kinetics. As displayed in Fig. S18a, GDY possesses a relatively smaller semicircle diameters upon comparison of graphite, demonstrating the superior K ion diffusivity kinetics in GDY. In addition, after calculation (Fig. S18b and Table S3), the σ (Warburg coefficient) value of GDY (10,240 Ω $S^{-1/2}$) was lower than that of the graphite (14,707 Ω $S^{-1/2}$) [70]. As demonstrated in Fig. S18c, the change of charge transfer resistances of the GDY electrode is much lower than that of the graphite either before or after cycling, indicating that a stable interface has been formed between the electrode and electrolyte, thus providing excellent cycling stability. Notably, the GDY electrodes show lower σ than the graphite electrode (Fig. S18d), revealing that GDY delivers a higher K^+ diffusion coefficient.

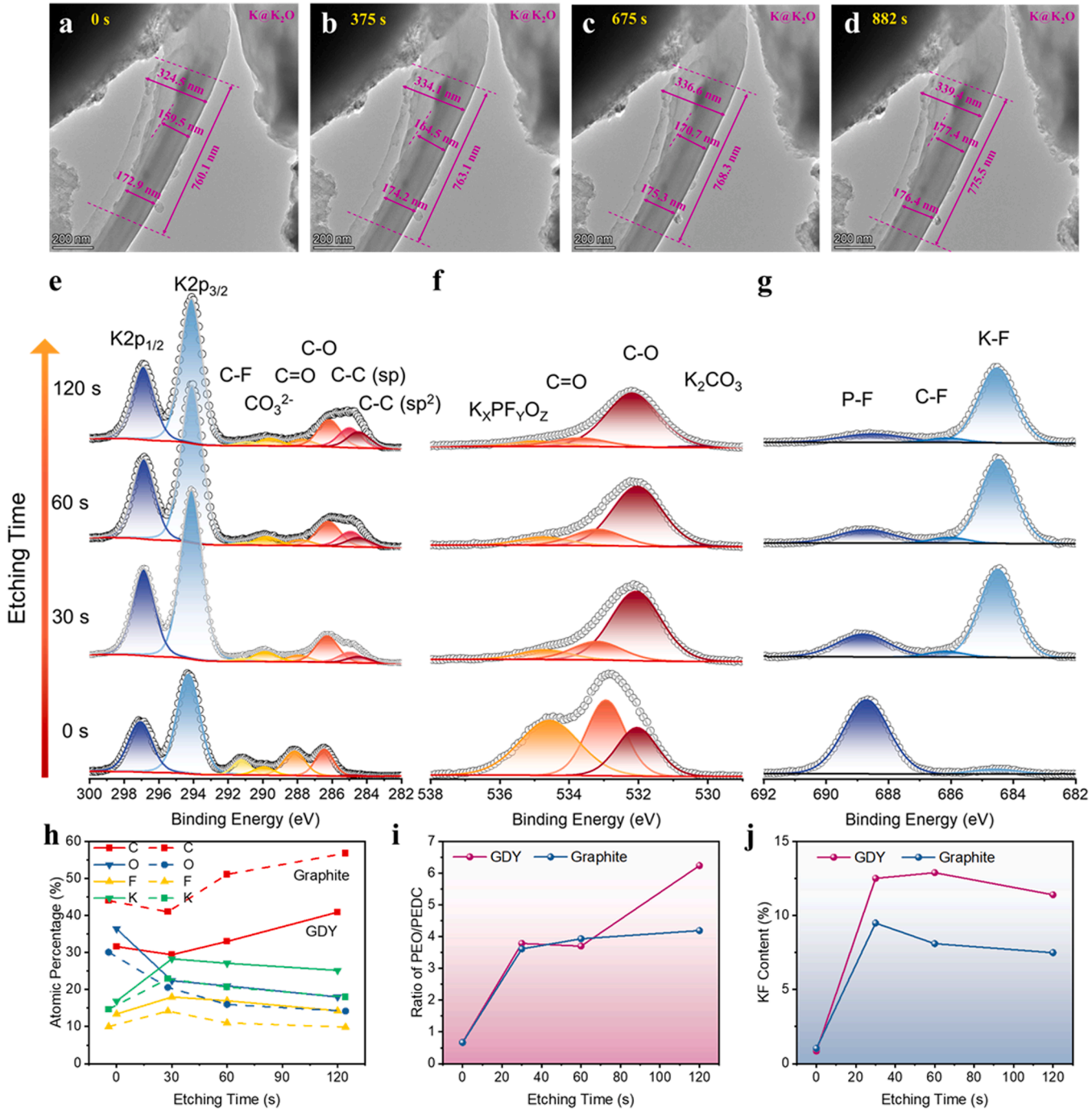

Fig. 5. (*a* − *d*) Time−lapse TEM images for a single GDY electrode during first potassiation process. (*e* − *j*) Depth profiling XPS analysis (normalized according to the relative peak intensity of the XPS spectrum) of the SEI chemistry after 10 cycles with sputtering time 0, 30, 60 and 120 s. GDY electrode retrieved from GDY/K half−cell charged to 3.0 V: (e) C 1 s & K 2p, (f) O 1 s and (g) F 1 s. (h) Quantified atomic composition ratios of the SEI obtained by XPS spectra for the GDY and graphite anodes cycled. (i) Ratio of PEO to PEDC in SEI based on O 1 s spectra f at different sputtering times. (j) Ratio of KF in SEI based on F 1 s spectra f at different sputtering times.

2.5. Structural evolution and interfacial chemistry of the GDY electrolyte interface

To clearly performs the dynamic evolution mechanism of GDY during the cycling process, a schematic illustration of self-regulating ion transport channel is shown in Fig. 4g. At the initial of discharge state, the interlayer spacing and pore size are increased due to the K^+ embedded and the conversion of alkyne−alkene bonds. In the further discharge process, more interlayer K^+ is adsorbed into the 18−C hexagon pores, resulting in an increase of pore size and a decrease interlayer spacing. During the charging process, partially intercalated or absorbed K^+ is removed, with the simultaneous decrease of the pore size and layer spacing. Afterward, K^+ in the triangular hole is released into interlayer and then extracted, corresponding to the increase of layer spacing and the expanded pores gradually return to the original state.

Real−time observation of potassiation process is the key to study the mechanism of electrochemical reaction. To clarify the microstructure evolution of GDY electrode during potassiation, a solid−state *K*−GDY nanobattery was assembled inside a TEM for in situ electrochemical experiments [71]. A bias potential of −3 V is then applied to the 2D GDY layer to induce the potassiation process. Fig. 5*a*−*d* show the time−−resolved TEM images during first potassiation captured from in situ TEM videos (Movie S1). With the continuous insertion of K^+, significant K accumulation can be observed on the reaction front with slight size expanding from 324.5 to 339.4 nm with an expansion rate of 4.5% (Fig. 5a–d). The regular 2D GDY plane framework is selected to study which can obtained exact volume change. By measuring the width and length of 2D GDY sheet in potassiation from 0 to 882 s, the length of 159.5, 172.9, 760.1 nm are gradually expanded to 177.4, 176.4, 775.5 nm (8.6 % expansion), confirming the rigid structure stability of GDY. These results clearly demonstrate the reliable structural stability of GDY during the potassiation process, with its volume expansion much smaller than that of graphite (theoretical volume expansion of 60 %). This is due to the intelligent adjustable structure brought about by chemical bond conversion, which reduces volume expansion and stress accumulation. Moreover, the morphology of GDY and graphite electrodes after 500 cycles were characterized by SEM (Fig. S19). There were severe huge cracks on graphite electrode, suggesting that the electrode undergoes a large volumetric change during cycling process. In addition, the slow K^+ diffusion can lead to local aggregation of ions and electrons on electrode surface, which induces an uneven and drastic potassiaiton reaction with great stress at the surface of graphite. In comparison, the electrode of GDY exhibits integral and smooth surface. Moreover, TEM images of electrodes after 500 cycles were also shown in Fig. S20. GDY presented an ultra−thin SEI layer. On the contrary, the SEI film of graphite is discontinuous, thick, and unstable. In a word, in/*ex situ* TEM with SEM confirm that the self−regulating *K*+ channels based on reversible chemical bond conversion can effectively stabilize electrode structure and withstand volume expansion.

Furthermore, the depth−profiling XPS were conducted to analyze the composition and of SEI formed in the electrode. The GDY electrode presented the stronger K 2p peak and weaker C—C peak in C 1 s photoelectron spectra with different Ar^+ bombardment times (Fig. 5e). After 30 s of ion sputtering, the C1s spectrum shows the emergence of the sp-C peak at 285.1 eV, which intensity increases with prolonged sputtering time. This indicates that the surface of GDY generates a thin SEI layer, consistent with TEM images of the cycled GDY (Fig. S20). The C 1 s spectra of graphite (Fig. S21a) exhibits a stronger peak at ~286.2 eV (RC—*O*—*K*) derived from solvent reduction appears in electrolyte, and the peak intensities is always stronger than GDY electrode upon Ar^+ ion bombardment [72]. This corroborates that the continuous consumption of electrolyte on the graphite surface forming much thicker SEI compared with GDY. As shown in Fig. 5h, GDY−derived SEI delivers the higher amounts of K and F element throughout whole probing depth, whereas the C element is lower compared with graphite, demonstrating the SEI mainly inorganic components while less organic components. The deconvoluted peak of O1s (Fig. 5c) at 532.0 eV (C—O) is attributed to the $-(CH_2CH_2O)_n-$ (assigned to (poly(ethylene oxide) oligomers, PEO), and $-OCO_2K$ is identified at 533.2 eV (C═O) (assigned to potassium ethylene decarbonate, PEDC). PEO has excellent electrochemical stability and anti−deformation ability, which could significantly increase the structural stability of SEI layer and reduce the electrolyte consumption [73]. In contrast, PEDC is easily decomposed to RCH_2OK or K_2CO_3 upon long cycling, continuously generating unstable SEI layers [74]. The ratio of PEO/PEDC (Fig. 5i) demonstrated that the outer SEI layers of GDY and graphite show similar organic content with the previous etching times, however, much more PEO are found near the GDY anode. More PEDC was formed with respect to PEO in graphite inner SEI, which gradually forms to the much thicker SEI layer. As shown in Fig. 5j, the inorganic content of KF in GDY is much higher across the whole−time step, which improves electrical conductivity and possess better mechanical strength to accommodate large volume changes. According to XPS results, GDY delivered organic (near the electrolyte)−inorganic (near the anode) heterogeneous SEI structures, implying that side−effect of solvent reduction is significantly suppressed [75]. Furthermore, the intrinsic fast ion diffusion kinetics is beneficial to generate a dense, robust, and high ionic conductive SEI, which contribute to exceptional interface stability.

2.6. DFT calculations

DFT calculations are performed to investigate the potassium storage model of GDY and influence mechanism of self−regulating ion channels. Before constructing the adsorption structure of only single K was added, and four possible configurations were selected and determined through appropriate binding energy. As shown in Fig. 6a-d, the adsorption energy (Ea) of K atom at the different positions of diacetylenic groups or above the benzene ring *K*−adsorption structures are calculated to be −1.77 eV, −1.79 eV, −1.94 eV respectively, to evaluate the *K*−adsorption ability. The center of triangular−like pores has the stronger interaction (−2.66 eV) with K than that of others sites, which is a more energetically favorable adsorption site. Electron density difference is calculated to analyze the bonding characteristic of adsorbed K atoms. As shown in Fig. 6e-f, an evident charge depletion near the adsorbed K atom can be observed in all three structures, suggesting transfer of charge from the adsorbed K to the neighboring C atom. The charge accumulation is more around the middle of the diacetylenic linkage in the molecular plane (Fig. 6g) which could further confirm the function of the sp−C in the storage of K. Moreover, the transport of charge density (−0.87 eV) of K atom at the center of 18−C skeleton of ion channels is smaller than that at the top of the benzene ring and alkyne bond (−0.90 eV, −0.91 eV), suggesting less charge transfer from the adsorbed K to the diacetylenic linkage, which is beneficial to migration of K. Therefore, it can be concluded that K has less charge transfer in ion channels, which proves the lower out−of−plane transport barrier and enhances the ion diffusion kinetics.

As shown in the electron localization function (ELF) analysis (Fig. 6h), the electron density distribution of K and GDY 18−C triangular pores has little change compared to the undoped configuration, suggesting the weak electron interactions. Based on the above discussion, the optimized configuration for the maximum K storage in GDY single−layer model is proposed. As depicted in Fig. 6i and Fig. S22, the 38 carbon atoms configurational unit can accommodate 14 K atoms with the specific capacity is significantly increased (1736 mAh g^{-1}) compared to graphite (575 mAh g^{-1}). It should be noted that the calculated theoretical capacity is much higher than the measured, and this occasion has been also reported in GDY materials for other batteries. The larger theoretical capacity in the calculation results is to explain the potassium storage mechanism of signal−layer GDY, without considering the effect of K shared by multi−layer GDY structures. As the higher K loadings on the monolayer GDY, distortion of the triangular pores accompanies by the formation of C4 ring and alkyne−alkene structures when reaches 14

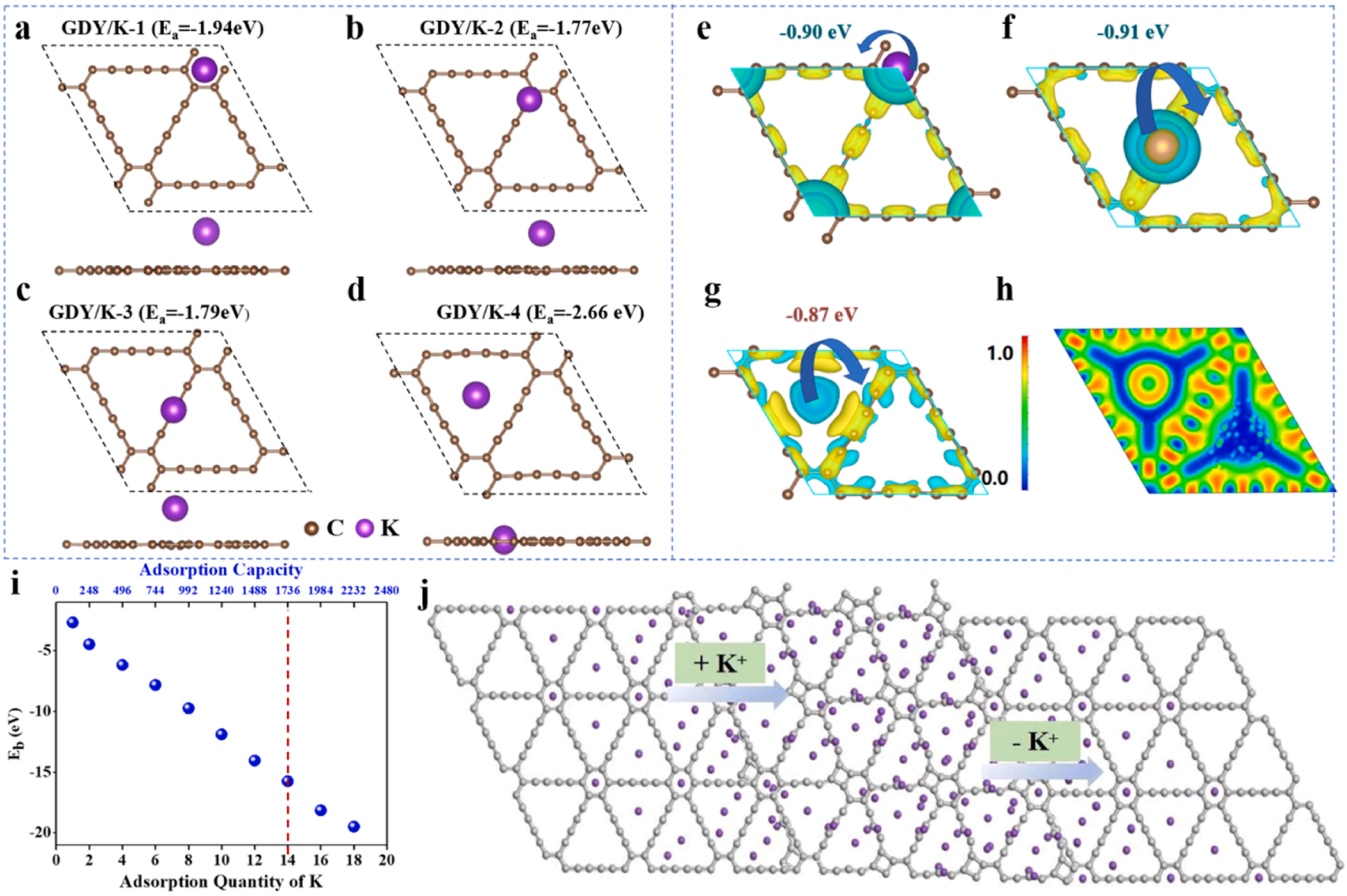

Fig. 6. Density functional theory (DFT) calculations. Top (left) and side (right) view K atom adsorbed on (a) center of in−plane benzene ring, (b) above the alkene, (c) above the diacetylenic groups and (d) center of in−plane triangular pores and corresponding adsorption energy. Electron density differences of a single K atom absorbed (e) center of in−plane benzene ring, (f) above the butadiyne groups and (g) center of in−plane triangular pores structures. The isosurfaces are 0.001 electron bohr^{-3}. Blue and yellow domains represent depleted electrons and accumulated electrons, respectively. (h) The local electronic structure of K atoms and GDY. (i) Calculated binding energy of *K*−ion adsorption, adsorption quantity, and the corresponding specific capacity. (j) The reversibility along the removing of K atoms in DFT calculations.

K atoms (Fig. S23). Due to the alkyne−*K* interaction, π−electrons transfer from alkyne to K, resulting in the formation of alkene and 18−C pore expansion. After removing all K atoms, the deformed GDY returned to the original state, demonstrating the reversibility of its structure (Fig. 6j).

3. Conclusion

In summary, we demonstrate a new strategy to overcome the terrible diffusion dynamics and volume expansion due to the large size of K^+. A series of kinetics study results indicate the dynamic evolution mechanism of the self−regulating ion channels, which is regulating K^+ transport channels by the reversible conversion of alkyne−alkene complex of GDY. Through in situ Raman, *ex situ* XPS and DFT calculation, this self-regulating ion channel promotes the out−of−plane K^+ migration perpendicular to 2D plane and improve ion transport kinetics. *In situ* TEM results verify the GDY with unique ion channel could effectively relieve volume variation and maintain structural integrity to benefit exceptional cycling stability. Based on this, GDY delivers an impressive capacity of 202 mAh g^{-1} at current density of 100 mA g^{-1} after 2100 cycles and ultra−long cycling stability with a decay of 0.012% per cycle, corresponding to a runtime of up to 380 days. This work offers a new perspective to regulate molecular carbon skeleton and its intrinsic transport kinetics for high-performance KIBs and next generation of electric energy storage systems.

CRediT authorship contribution statement

Wencong Feng: Methodology, Data curation, Formal analysis, Writing – original draft. **Chuanqi Pan:** Methodology, Data curation, Formal analysis. **Hong Wang:** Methodology, Software. **Biluan Zhang:** Software. **Wen Luo:** Methodology. **Chunli Shen:** Methodology. **Junjun Wang:** Data curation. **Chaojie Cheng:** Methodology, Formal analysis. **Xianmin Xv:** . **Ruohan Yu:** Software. **Yanbing Guo:** Conceptualization, Supervision. **Liqiang Mai:** Conceptualization, Supervision, Project administration, Funding acquisition, Writing – review & editing.

Declaration of Competing Interest

The authors declare that they have no known competing financial interests or personal relationships that could have appeared to influence the work reported in this paper.

Acknowledgements

This work was supported by the National Natural Science Foundation of China (51832004, 52127816), National Key Research and Development Program of China (2020YFA0715000), Hainan Provincial Joint Project of Sanya Yazhou Bay Science and Technology City (2021CXLH0007), Knowledge Innovation Program of Wuhan-Shugung Project (2022010801020289), the Open Foundation of State Key Laboratory of Advanced Technology for Materials Synthesis and Processing

(Wuhan University of Technology, 2019-KF-8).

Supplementary materials

Supplementary material associated with this article can be found, in the online version, at doi:10.1016/j.ensm.2023.102975.

References

[1] T. Hosaka, K. Kubota, A.S. Hameed, S. Komaba, Research Development on K-Ion Batteries, Chem. Rev. 120 (14) (2020) 6358–6466, https://doi.org/10.1021/acs.chemrev.9b00463.

[2] L. Jiang, Y. Lu, C. Zhao, L. Liu, J. Zhang, Q. Zhang, X. Shen, J. Zhao, X. Yu, H. Li, X. Huang, L. Chen, Y.-S. Hu, Building aqueous K-ion batteries for energy storage, Nat. Energy 4 (6) (2019) 495–503, https://doi.org/10.1038/s41560-019-0388-0.

[3] Y. Tian, G. Zeng, A. Rutt, T. Shi, H. Kim, J. Wang, J. Koettgen, Y. Sun, B. Ouyang, T. Chen, Z. Lun, Z. Rong, K. Persson, G. Ceder, Promises and Challenges of Next-Generation "Beyond Li-ion" Batteries for Electric Vehicles and Grid Decarbonization, Chem. Rev. 121 (3) (2021) 1623–1669, https://doi.org/10.1021/acs.chemrev.0c00767.

[4] J. Zheng, Y. Yang, X. Fan, G. Ji, X. Ji, H. Wang, S. Hou, M.R. Zachariah, C. Wang, Extremely stable antimony–carbon composite anodes for potassium-ion batteries, Energy Environ. Sci. 12 (2) (2019) 615–623, https://doi.org/10.1039/c8ee02836b.

[5] L. Wang, B. Zhang, B. Wang, S. Zeng, M. Zhao, X. Sun, Y. Zhai, L. Xu, In-situ Nano-Crystallization and Solvation Modulation to Promote Highly Stable Anode Involving Alloy/De-alloy for Potassium Ion Batteries, Angew. Chem. Int. Ed. 60 (28) (2021) 15381–15389, https://doi.org/10.1002/anie.202100654.

[6] F. Xu, Y. Zhai, E. Zhang, Q. Liu, G. Jiang, X. Xu, Y. Qiu, X. Liu, H. Wang, S. Kaskel, Ultrastable Surface-Dominated Pseudocapacitive Potassium Storage Enabled by Edge-Enriched N-Doped Porous Carbon Nanosheets, Angew. Chem. Int. Ed. 59 (44) (2020) 19460–19467, https://doi.org/10.1002/anie.202005118.

[7] X. Zhou, L. Chen, W. Zhang, J. Wang, Z. Liu, S. Zeng, R. Xu, Y. Wu, S. Ye, Y. Feng, X. Cheng, Z. Peng, X. Li, Y. Yu, Three-Dimensional Ordered Macroporous Metal-Organic Framework Single Crystal-Derived Nitrogen-Doped Hierarchical Porous Carbon for High-Performance Potassium-Ion Batteries, Nano Lett 19 (8) (2019) 4965–4973, https://doi.org/10.1021/acs.nanolett.9b01127.

[8] Y. Xu, C. Zhang, M. Zhou, Q. Fu, C. Zhao, M. Wu, Y. Lei, Highly nitrogen doped carbon nanofibers with superior rate capability and cyclability for potassium ion batteries, Nat. Commun. 9 (1) (2018) 1720, https://doi.org/10.1038/s41467-018-04190-z.

[9] J. Ge, L. Fan, A.M. Rao, J. Zhou, B. Lu, Surface-substituted Prussian blue analogue cathode for sustainable potassium-ion batteries, Nat. Sustain. 5 (3) (2021) 225–234, https://doi.org/10.1038/s41893-021-00810-7.

[10] W. Zhang, Z. Cao, W. Wang, E. Alhajji, A.H. Emwas, P. Costa, L. Cavallo, H. N. Alshareef, A Site-Selective Doping Strategy of Carbon Anodes with Remarkable K-Ion Storage Capacity, Angew. Chem. Int. Ed. 59 (11) (2020) 4448–4455, https://doi.org/10.1002/anie.201913368.

[11] Y. Liu, Y.X. Lu, Y.S. Xu, Q.S. Meng, J.C. Gao, Y.G. Sun, Y.S. Hu, B.B. Chang, C. T. Liu, A.M. Cao, Pitch-Derived Soft Carbon as Stable Anode Material for Potassium Ion Batteries, Adv. Mater. 32 (17) (2020), e2000505, https://doi.org/10.1002/adma.202000505.

[12] W. Yang, J. Zhou, S. Wang, W. Zhang, Z. Wang, F. Lv, K. Wang, Q. Sun, S. Guo, Freestanding film made by necklace-like N-doped hollow carbon with hierarchical pores for high-performance potassium-ion storage, Energy Environ. Sci. 12 (5) (2019) 1605–1612, https://doi.org/10.1039/c9ee00536f.

[13] D.S. Bin, X.J. Lin, Y.G. Sun, Y.S. Xu, K. Zhang, A.M. Cao, L.J. Wan, Engineering Hollow Carbon Architecture for High-Performance K-Ion Battery Anode, J. Am. Chem. Soc. 140 (23) (2018) 7127–7134, https://doi.org/10.1021/jacs.8b02178.

[14] Z. Jian, W. Luo, X. Ji, Carbon Electrodes for K-Ion Batteries, J. Am. Chem. Soc. 137 (36) (2015) 11566–11569, https://doi.org/10.1021/jacs.5b06809.

[15] H. Zhang, W. Li, J. Pan, Z. Sun, B. Xiao, W. Ye, C. Ke, H. Gao, Y. Cheng, Q. Zhang, M.-S. Wang, Synergistic coupling of amorphous carbon and graphitic domains toward high-rate and long-life K+ storage, J. Energy Chem. 73 (2022) 533–541, https://doi.org/10.1016/j.jechem.2022.07.004.

[16] J. Liu, T. Yin, B. Tian, B. Zhang, C. Qian, Z. Wang, L. Zhang, P. Liang, Z. Chen, J. Yan, X. Fan, J. Lin, X. Chen, Y. Huang, K.P. Loh, Z.X. Shen, Unraveling the Potassium Storage Mechanism in Graphite Foam, Adv. Energy. Mater. 9 (22) (2019), https://doi.org/10.1002/aenm.201900579.

[17] Y. Chen, B. Xi, M. Huang, L. Shi, S. Huang, N. Guo, D. Li, Z. Ju, S. Xiong, Defect-Selectivity and "Order-in-Disorder" Engineering in Carbon for Durable and Fast Potassium Storage, Adv. Mater. 34 (7) (2022), e2108621, https://doi.org/10.1002/adma.202108621.

[18] Y. Qian, S. Jiang, Y. Li, Z. Yi, J. Zhou, J. Tian, N. Lin, Y. Qian, Water-Induced Growth of a Highly Oriented Mesoporous Graphitic Carbon Nanospring for Fast Potassium-Ion Adsorption/Intercalation Storage, Angew. Chem. Int. Ed. 58 (50) (2019) 18108–18115, https://doi.org/10.1002/anie.201912287.

[19] J. Zhang, Z. Cao, L. Zhou, G. Liu, G.-T. Park, L. Cavallo, L. Wang, H.N. Alshareef, Y.-K. Sun, J. Ming, Model-Based Design of Graphite-Compatible Electrolytes in Potassium-Ion Batteries, ACS Energy Lett 5 (8) (2020) 2651–2661, https://doi.org/10.1021/acsenergylett.0c01401.

[20] L. Fan, Q. Liu, S. Chen, K. Lin, Z. Xu, B. Lu, Potassium-Based Dual Ion Battery with Dual-Graphite Electrode, Small 13 (30) (2017), https://doi.org/10.1002/smll.201701011.

[21] S. Liu, J. Mao, L. Zhang, W.K. Pang, A. Du, Z. Guo, Manipulating the Solvation Structure of Nonflammable Electrolyte and Interface to Enable Unprecedented Stability of Graphite Anodes beyond 2 Years for Safe Potassium-Ion Batteries, Adv. Mater. 33 (1) (2021), https://doi.org/10.1002/adma.202006313.

[22] L. Fan, R. Ma, Q. Zhang, X. Jia, B. Lu, Graphite Anode for a Potassium-Ion Battery with Unprecedented Performance, Angew. Chem. Int. Ed. 58 (31) (2019) 10500–10505, https://doi.org/10.1002/anie.201904258.

[23] W. Yang, J. Zhou, S. Wang, Z. Wang, F. Lv, W. Zhang, W. Zhang, Q. Sun, S. Guo, A Three-Dimensional Carbon Framework Constructed by N/S Co-doped Graphene Nanosheets with Expanded Interlayer Spacing Facilitates Potassium Ion Storage, ACS Energy Lett 5 (5) (2020) 1653–1661, https://doi.org/10.1021/acsenergylett.0c00413.

[24] Y. Qian, S. Jiang, Y. Li, Z. Yi, J. Zhou, J. Tian, N. Lin, Y. Qian, Understanding mesopore volume-enhanced extra-capacity: optimizing mesoporous carbon for high-rate and long-life potassium-storage, Energy Storage Mater 29 (2020) 341–349, https://doi.org/10.1016/j.ensm.2020.04.026.

[25] L. Zhong, W. Zhang, S. Sun, L. Zhao, W. Jian, X. He, Z. Xing, Z. Shi, Y. Chen, H. N. Alshareef, X. Qiu, Engineering of the Crystalline Lattice of Hard Carbon Anodes Toward Practical Potassium-Ion Batteries, Adv. Funct. Mater. 33 (8) (2022), https://doi.org/10.1002/adfm.202211872.

[26] Q. Zhang, X. Cheng, C. Wang, A.M. Rao, B. Lu, Sulfur-assisted large-scale synthesis of graphene microspheres for superior potassium-ion batteries, Energy Environ. Sci. 14 (2) (2021) 965–974, https://doi.org/10.1039/d0ee03203d.

[27] Y. Zhao, J. Zhu, S.J.H. Ong, Q. Yao, X. Shi, K. Hou, Z.J. Xu, L. Guan, High-rate and ultralong cycle-life potassium ion batteries enabled by in situ engineering of yolk-shell FeS2@C structure on graphene matrix, Adv. Energy. Mater. 8 (36) (2018), https://doi.org/10.1002/aenm.201802565.

[28] X. Hu, Y. Liu, J. Chen, L. Yi, H. Zhan, Z. Wen, Fast redox kinetics in Bi-Heteroatom doped 3D porous carbon nanosheets for high-performance hybrid potassium-ion battery capacitors, Adv. Energy. Mater. 9 (42) (2019), https://doi.org/10.1002/aenm.201901533.

[29] C. Lu, Z. Sun, L. Yu, X. Lian, Y. Yi, J. Li, Z. Liu, S. Dou, J. Sun, Enhanced kinetics harvested in heteroatom dual-doped graphitic hollow architectures toward high rate printable potassium-ion batteries, Adv. Energy. Mater. 10 (28) (2020), https://doi.org/10.1002/aenm.202001161.

[30] J. Wu, X. Zhang, Z. Li, C. Yang, W. Zhong, W. Li, C. Zhang, N. Yang, Q. Zhang, X. Li, Toward high-performance capacitive potassium-ion storage: a superior anode material from silicon carbide-derived carbon with a well-developed pore structure, Adv. Funct. Mater. 30 (40) (2020), https://doi.org/10.1002/adfm.202004348.

[31] Z. Tan, K. Ni, G. Chen, W. Zeng, Z. Tao, M. Ikram, Q. Zhang, H. Wang, L. Sun, X. Zhu, X. Wu, H. Ji, R.S. Ruoff, Y. Zhu, Incorporating pyrrolic and pyridinic nitrogen into a porous carbon made from C60 molecules to obtain superior energy storage, Adv. Mater. 29 (8) (2017), https://doi.org/10.1002/adma.201603414.

[32] H. Huang, R. Xu, Y. Feng, S. Zeng, Y. Jiang, H. Wang, W. Luo, Y. Yu, Sodium/potassium-ion batteries: boosting the rate capability and cycle life by combining morphology, defect and structure engineering, Adv. Mater. 32 (8) (2020), e1904320, https://doi.org/10.1002/adma.201904320.

[33] Y. Qian, S. Jiang, Y. Li, Z. Yi, J. Zhou, T. Li, Y. Han, Y. Wang, J. Tian, N. Lin, Y. Qian, In situ revealing the electroactivity of PO and PC bonds in hard carbon for high-capacity and long-life Li/K-Ion batteries, Adv. Energy. Mater. 9 (34) (2019), https://doi.org/10.1002/aenm.201901676.

[34] J. Chen, Y. Cheng, Q. Zhang, C. Luo, H.Y. Li, Y. Wu, H. Zhang, X. Wang, H. Liu, X. He, J. Han, D.L. Peng, M. Liu, M.S. Wang, Designing and understanding the superior potassium storage performance of Nitrogen/Phosphorus co-doped hollow porous bowl-like carbon anodes, Adv. Funct. Mater. 31 (1) (2020), https://doi.org/10.1002/adfm.202007158.

[35] X. Zhou, L. Wang, Y. Yao, Y. Jiang, R. Xu, H. Wang, X. Wu, Y. Yu, Integrating conductivity, captivity, and immobility ability into N/O dual-doped porous carbon nanocage anchored with CNT as an effective Se host for advanced K-Se battery, Adv. Funct. Mater. 30 (43) (2020), https://doi.org/10.1002/adfm.202003871.

[36] H. Li, Z. Cheng, Q. Zhang, A. Natan, Y. Yang, D. Cao, H. Zhu, Bacterial-derived, compressible, and hierarchical porous carbon for high-performance potassium-ion batteries, Nano Lett 18 (11) (2018) 7407–7413, https://doi.org/10.1021/acs.nanolett.8b03845.

[37] D. Li, L. Dai, X. Ren, F. Ji, Q. Sun, Y. Zhang, L. Ci, Foldable potassium-ion batteries enabled by free-standing and flexible SnS2@C nanofibers, Energy Environ. Sci. 14 (1) (2021) 424–436, https://doi.org/10.1039/d0ee02919j.

[38] J.F. Wu, W. Zhou, Z. Wang, W.W. Wang, X. Lan, H. Yan, T. Shi, R. Hu, X. Cui, C. Xu, X. He, B.W. Mao, T. Zhang, J. Liu, Building K-C anode with ultrahigh self-diffusion coefficient for solid state potassium metal batteries operating at -20 to 120 °C, Adv. Mater. (2023), e2209833, https://doi.org/10.1002/adma.202209833.

[39] Y. Liu, Q. Liu, C. Jian, D. Cui, M. Chen, Z. Li, T. Li, T. Nilges, K. He, Z. Jia, C. Zhou, Red-phosphorus-impregnated carbon nanofibers for sodium-ion batteries and liquefaction of red phosphorus, Nat. Commun. 11 (1) (2020) 2520, https://doi.org/10.1038/s41467-020-16077-z.

[40] G. Li, Y. Li, H. Liu, Y. Guo, Y. Li, D. Zhu, Architecture of graphdiyne nanoscale films, Chem Commun. 46 (19) (2010) 3256–3258, https://doi.org/10.1039/b922733d.

[41] R. Matsuoka, R. Sakamoto, K. Hoshiko, S. Sasaki, H. Masunaga, K. Nagashio, H. Nishihara, Crystalline Graphdiyne nanosheets produced at a gas/liquid or Liquid/Liquid interface, J. Am. Chem. Soc. 139 (8) (2017) 3145–3152, https://doi.org/10.1021/jacs.6b12776.

[42] T. Lu, J. He, R. Li, K. Wang, Z. Yang, X. Shen, Y. Li, J. Xiao, C. Huang, Adjusting the interface structure of graphdiyne by H and F co-doping for enhanced capacity and stability in Li-ion battery, Energy Storage Mater 29 (2020) 131–139, https://doi.org/10.1016/j.ensm.2020.04.013.
[43] H. Shang, Z. Zuo, L. Li, F. Wang, H. Liu, Y. Li, Y. Li, Ultrathin Graphdiyne nanosheets grown in situ on copper nanowires and their performance as lithium-ion battery anodes, Angew. Chem. Int. Ed. 57 (3) (2018) 774–778, https://doi.org/10.1002/anie.201711366.
[44] X. Gao, Z. Zuo, F. Wang, Q. Chang, H. Pan, L. Li, F. He, Y. Li, Controlling precise voids in the ion-selective carbon shell for zero-strain electrode, Energy Storage Mater 45 (2022) 110–118, https://doi.org/10.1016/j.ensm.2021.11.035.
[45] J. He, T. Lu, K. Wang, X. Wang, X. Li, X. Shen, J. Gao, W. Si, Z. Yang, C. Huang, Rational construction of advanced potassium ion diffusion and storage matrix, Adv. Funct. Mater. 31 (5) (2020), https://doi.org/10.1002/adfm.202005933.
[46] T. Wang, J. Zhao, L. Qi, G. Li, W. Yang, Y. Li, Ultrathin graphdiyne oxide-intercalated MXene: a new heterostructure with interfacial synergistic effect for high performance lithium-ion storage, Energy Storage Mater 54 (2023) 10–19, https://doi.org/10.1016/j.ensm.2022.10.022.
[47] Y. Yi, J. Li, W. Zhao, Z. Zeng, C. Lu, H. Ren, J. Sun, J. Zhang, Z. Liu, Temperature-mediated engineering of graphdiyne framework enabling high-performance potassium storage, Adv. Funct. Mater. 30 (31) (2020), https://doi.org/10.1002/adfm.202003039.
[48] Z. Yang, Y. Song, C. Zhang, J. He, X. Li, X. Wang, N. Wang, Y. Li, C. Huang, Porous 3D silicon-diamondyne blooms excellent storage and diffusion properties for Li, Na, and K Ions, Adv. Energy. Mater. 11 (33) (2021), https://doi.org/10.1002/aenm.202101197.
[49] J. Li, Y. Yi, X. Zuo, B. Hu, Z. Xiao, R. Lian, Y. Kong, L. Tong, R. Shao, J. Sun, J. Zhang, Graphdiyne/Graphene/Graphdiyne sandwiched carbonaceous anode for potassium-ion batteries, ACS Nano 16 (2) (2022) 3163–3172, https://doi.org/10.1021/acsnano.1c10857.
[50] L. Li, Z. Zuo, F. Wang, J. Gao, A. Cao, F. He, Y. Li, In situ coating graphdiyne for high-energy-density and stable organic cathodes, Adv. Mater 32 (14) (2020), e2000140, https://doi.org/10.1002/adma.202000140.
[51] Y. Fang, Y. Liu, L. Qi, Y. Xue, Y. Li, 2D graphdiyne: an emerging carbon material, Chem. Soc. Rev. 51 (7) (2022) 2681–2709, https://doi.org/10.1039/d1cs00592h.
[52] C. Pan, C. Wang, Y. Fang, Y. Zhu, H. Deng, Y. Guo, Graphdiyne: an emerging two-dimensional (2D) carbon material for environmental remediation, Environ. Sci. Nano 8 (7) (2021) 1863–1885, https://doi.org/10.1039/d1en00231g.
[53] C. Huang, Y. Li, N. Wang, Y. Xue, Z. Zuo, H. Liu, Y. Li, Progress in research into 2D Graphdiyne-based materials, Chem. Rev. 118 (16) (2018) 7744–7803, https://doi.org/10.1021/acs.chemrev.8b00288.
[54] H. Yan, P. Yu, G. Han, Q. Zhang, L. Gu, Y. Yi, H. Liu, Y. Li, L. Mao, High-yield and damage-free exfoliation of layered graphdiyne in aqueous phase, Angew. Chem. Int. Ed. 58 (3) (2019) 746–750, https://doi.org/10.1002/anie.201809730.
[55] C. Pan, C. Wang, X. Zhao, P. Xu, F. Mao, J. Yang, Y. Zhu, R. Yu, S. Xiao, Y. Fang, H. Deng, Z. Luo, J. Wu, J. Li, S. Liu, S. Xiao, L. Zhang, Y. Guo, Neighboring sp-Hybridized carbon participated molecular oxygen activation on the interface of sub-nanocluster CuO/Graphdiyne, J. Am. Chem. Soc. 144 (11) (2022) 4942–4951, https://doi.org/10.1021/jacs.1c12772.
[56] L. Hui, X. Zhang, Y. Xue, X. Chen, Y. Fang, C. Xing, Y. Liu, X. Zheng, Y. Du, C. Zhang, F. He, Y. Li, Highly dispersed platinum chlorine atoms anchored on gold quantum dots for a highly efficient electrocatalyst, J. Am. Chem. Soc. 144 (4) (2022) 1921–1928, https://doi.org/10.1021/jacs.1c12310.
[57] X. Gao, H. Liu, D. Wang, J. Zhang, Graphdiyne: synthesis, properties, and applications, Chem. Soc. Rev. 48 (3) (2019) 908–936, https://doi.org/10.1039/c8cs00773j.
[58] Y. Gao, Y. Xue, L. Qi, C. Xing, X. Zheng, F. He, Y. Li, Rhodium nanocrystals on porous graphdiyne for electrocatalytic hydrogen evolution from saline water, Nat. Commun. 13 (1) (2022) 5227, https://doi.org/10.1038/s41467-022-32937-2.
[59] Y. Gao, Y. Xue, F. He, Y. Li, Controlled growth of a high selectivity interface for seawater electrolysis, Proc. Natl. Acad. Sci. U S A 119 (36) (2022), e2206946119, https://doi.org/10.1073/pnas.2206946119.
[60] J. An, H. Zhang, L. Qi, G. Li, Y. Li, Self-expanding ion-transport channels on anodes for fast-charging lithium-ion batteries, Angew. Chem. Int. Ed. 61 (7) (2022), e202113313, https://doi.org/10.1002/anie.202113313.
[61] Y. Wang, J. An, L. Qi, Y. Xue, G. Li, Q. Lyu, W. Yang, Y. Li, Synthesis of crystalline Phosphine-Graphdiyne with self-adaptive p-pi conjugation, J. Am. Chem. Soc. 145 (2) (2023) 864–872, https://doi.org/10.1021/jacs.2c09209.
[62] J. Li, X. Han, D. Wang, L. Zhu, M.H. Ha-Thi, T. Pino, J. Arbiol, L.Z. Wu, M. Nawfal Ghazzal, A deprotection-free method for high-yield synthesis of Graphdiyne powder with in situ formed CuO nanoparticles, Angew. Chem. Int. Ed. 61 (43) (2022), e202210242, https://doi.org/10.1002/anie.202210242.
[63] F. Wang, J. An, H. Shen, Z. Wang, G. Li, Y. Li, Gradient Graphdiyne induced copper and oxygen vacancies in Cu(0.95) V(2) O(5) anodes for fast-charging lithium-ion batteries, Angew. Chem. Int. Ed. 62 (7) (2023), e202216397, https://doi.org/10.1002/anie.202216397.
[64] H. Shang, Z. Zuo, L. Yu, F. Wang, F. He, Y. Li, Low-temperature growth of all-carbon graphdiyne on a silicon anode for high-performance lithium-ion batteries, Adv. Mater. 30 (27) (2018), e1801459, https://doi.org/10.1002/adma.201801459.
[65] X. Liang, X. Li, Q. Xiang, S. Zhang, Y. Cao, M. Han, Y. Zhang, C. Zhou, Y. Xu, C. Mao, W. Li, J. Sun, Surficial oxidation of phosphorus for strengthening interface interaction and enhancing lithium-storage performance, Nano Lett 22 (23) (2022) 9335–9342, https://doi.org/10.1021/acs.nanolett.2c03038.
[66] L. Wang, J. Zou, S. Chen, G. Zhou, J. Bai, P. Gao, Y. Wang, X. Yu, J. Li, Y.-S. Hu, H. Li, TiS2 as a high performance potassium ion battery cathode in ether-based electrolyte, Energy Storage Mater 1 (2018) 216–222, https://doi.org/10.1016/j.ensm.2017.12.018.
[67] C. Choi, D.S. Ashby, D.M. Butts, R.H. DeBlock, Q. Wei, J. Lau, B. Dunn, Achieving high energy density and high power density with pseudocapacitive materials, Nat. Rev. Mater. 5 (1) (2019) 5–19, https://doi.org/10.1038/s41578-019-0142-z.
[68] M. Liu, F. Wu, Y. Gong, Y. Li, Y. Li, X. Feng, Q. Li, C. Wu, Y. Bai, Interfacial-catalysis-enabled layered and inorganic-rich SEI on hard carbon anodes in ester electrolytes for sodium-ion batteries, Adv. Mater. 35 (29) (2023), https://doi.org/10.1002/adma.202300002.
[69] L. Deng, K. Goh, F.-D. Yu, Y. Xia, Y.-S. Jiang, W. Ke, Y. Han, L.-F. Que, J. Zhou, Z.-B. Wang, Self-optimizing weak solvation effects achieving faster low-temperature charge transfer kinetics for high-voltage Na3V2(PO4)2F3 cathode, Energy Storage Mater 44 (2022) 82–92, https://doi.org/10.1016/j.ensm.2021.10.012.
[70] X. Liang, X. Wang, G. Li, Q. Xiang, C. Zhou, A. Chen, X. Li, S. Zhang, Y. Cao, M. Han, C. Han, H. Gong, H. Wang, Y. Zhang, J. Sun, Unlocking the side reaction mechanism of phosphorus anode with binder and the development of a multifunctional binder for enhancing the performance, J. Power Sources 541 (2022), https://doi.org/10.1016/j.jpowsour.2022.231686.
[71] W. Feng, H. Wang, Y. Jiang, H. Zhang, W. Luo, W. Chen, C. Shen, C. Wang, J. Wu, L. Mai, A strain-relaxation red phosphorus freestanding anode for non-aqueous potassium ion batteries, Adv. Energy. Mater. 12 (7) (2022), https://doi.org/10.1002/aenm.202103343.
[72] K. Lei, C. Wang, L. Liu, Y. Luo, C. Mu, F. Li, J. Chen, A porous network of Bismuth used as the anode material for high-energy-density potassium-ion batteries, Angew. Chemie-Int. Ed. 57 (17) (2018) 4687–4691, https://doi.org/10.1002/anie.201801389.
[73] W. Zhou, B. He, L. Quan, R. Li, Y. Chen, C. Fan, S. Chen, C. Xu, X. Fan, L. Xing, J. Liu, Binder chemistry dependent electrolyte reduction in potassium-ion batteries: a successive, two-step reduction way, Adv. Energy. Mater. 13 (2) (2022), https://doi.org/10.1002/aenm.202202874.
[74] Y. Mo, W. Zhou, K. Wang, K. Xiao, Y. Chen, Z. Wang, P. Tang, P. Xiao, Y. Gong, S. Chen, P. Gao, J. Liu, Engineering electrode/electrolyte interphase chemistry toward high-rate and long-life potassium ion full-cell, ACS Energy Lett 8 (2) (2023) 995–1002, https://doi.org/10.1021/acsenergylett.2c02659.
[75] Y. Chen, Z. Yu, P. Rudnicki, H. Gong, Z. Huang, S.C. Kim, J.C. Lai, X. Kong, J. Qin, Y. Cui, Z. Bao, Steric effect tuned ion solvation enabling stable cycling of high-voltage lithium metal battery, J. Am. Chem. Soc. 143 (44) (2021) 18703–18713, https://doi.org/10.1021/jacs.1c09006.